Electronic Supporting Information

Frozen Water NMR Lineshape Analysis Enables Absolute Polarization Quantification

Igor V. Koptyug[a], Quentin Stern[b], Sami Jannin[b] and Stuart J. Elliott[b,c,†]

[a] International Tomography Center, SB RAS, 3A Institutskaya St., Novosibirsk, 630090 Russia
[b] Univ. Lyon, CNRS, ENS Lyon, UCBL, Université de Lyon, CRMN UMR 5280, 69100 Villeurbanne, France
[c] Current Address: Molecular Sciences Research Hub, Imperial College London, London W12 0BZ, United Kingdom

Corresponding Author: [†]s.elliott@imperial.ac.uk

Contents

1. *Sample Formulation Optimization*

Table S1: Fraction optimization of H_2O/DMSO-d_6 glassing mixture constituents.

H_2O Fraction	DMSO-d_6 Fraction	Glass (*y*/*n*)
1	1	*y*
1	2	*y*
1	3	*y*
1	5	*y*
1	6	*n*
1	7	*n*
1	8	*n*
1	19	*n*

These results indicate that the most optimally performing ratio of H_2O/DMSO-d_6 is 1:5. Glassing was determined by freezing 10 μL volumes in liquid nitrogen and visually inspecting bead sample glassiness by eye. It may also be the case that lower ratios of H_2O/DMSO-d_6 polarize to greater extents.

2. Derivation of Echo-Based Signal Intensity

Product operator formalism for the echo-based *rf*-pulse sequence shown in Figure 1b of the main text (taking *J*-coupling to be a proxy for dipolar coupling).

A) α_x - t_{echo} - β_y - t_{echo} - acq

$\sigma_{eq} = I_{1Z} + I_{2Z}$

1) First pulse α_x

$I_Z \rightarrow \cos(\alpha)I_Z + \sin(\alpha)I_Y$
$\sigma_1 = \cos(\alpha)I_{1Z} + \sin(\alpha)I_{1Y} + \cos(\alpha)I_{2Z} + \sin(\alpha)I_{2Y}$

2) Evolution under J-coupling

$I_Z \rightarrow I_Z$
$I_{1Y} \rightarrow \cos(\pi Jt)I_{1Y} - 2\sin(\pi Jt)I_{1X}I_{2Z}$
$I_{2Y} \rightarrow \cos(\pi Jt)I_{2Y} - 2\sin(\pi Jt)I_{1Z}I_{2X}$

$\sigma_2 = \cos(\alpha)(I_{1Z} + I_{2Z}) + \sin(\alpha)(\cos(\pi Jt)I_{1Y} - 2\sin(\pi Jt)I_{1X}I_{2Z}) + \sin(\alpha)(\cos(\pi Jt)I_{2Y} - 2\sin(\pi Jt)I_{1Z}I_{2X})$

3) Second pulse β_y

$I_Z \rightarrow \cos(\beta)I_Z - \sin(\beta)I_X$
$I_Y \rightarrow I_Y$
$I_X \rightarrow \cos(\beta)I_X + \sin(\beta)I_Z$
$I_{1X}I_{2Z} \rightarrow (\cos(\beta)I_{1X} + \sin(\beta)I_{1Z})(\cos(\beta)I_{2Z} - \sin(\beta)I_{2X})$
$I_{1Z}I_{2X} \rightarrow (\cos(\beta)I_{1Z} - \sin(\beta)I_{1X})(\cos(\beta)I_{2X} + \sin(\beta)I_{2Z})$

$\sigma_3(y) = \cos(\alpha)\cos(\beta)(I_{1Z} + I_{2Z})$
$- \cos(\alpha)\sin(\beta)I_{1X}$
$- \cos(\alpha)\sin(\beta)I_{2X}$
$+ \sin(\alpha)\cos(\pi Jt)I_{1Y}$
$+ \sin(\alpha)\cos(\pi Jt)I_{2Y}$
$- 2\sin(\alpha)\sin(\pi Jt)\cos(2\beta)I_{1X}I_{2Z}$
$- 2\sin(\alpha)\sin(\pi Jt)\cos(2\beta)I_{1Z}I_{2X}$
$+ 2\sin(\alpha)\sin(\pi Jt)\sin(2\beta)I_{1X}I_{2X}$
$- 2\sin(\alpha)\sin(\pi Jt)\sin(2\beta)I_{1Z}I_{2Z}$

4) Evolution under J-coupling

$I_Z \rightarrow I_Z$
$I_{1Y} \rightarrow \cos(\pi Jt)I_{1Y} - \sin(\pi Jt)2I_{1X}I_{2Z}$
$I_{2Y} \rightarrow \cos(\pi Jt)I_{2Y} - \sin(\pi Jt)2I_{1Z}I_{2X}$
$I_{1X} \rightarrow \cos(\pi Jt)I_{1X} + \sin(\pi Jt)2I_{1Y}I_{2Z}$
$I_{2X} \rightarrow \cos(\pi Jt)I_{2X} + \sin(\pi Jt)2I_{1Z}I_{2Y}$
$I_{1X}I_{2X} \rightarrow I_{1X}I_{2X}$
$I_{1Z}I_{2Z} \rightarrow I_{1Z}I_{2Z}$
$I_{1X}I_{2Z} \rightarrow \cos(\pi Jt)I_{1X}I_{2Z} + 0.5\sin(\pi Jt)I_{1Y}$

$I_{1Z}I_{2X} \rightarrow cos(\pi Jt)I_{1Z}I_{2X} + 0.5sin(\pi Jt)I_{2Y}$

$\sigma_4 (y) = cos(\alpha)cos(\beta)I_{1Z}$
$+ cos(\alpha)cos(\beta)I_{2Z}$
$+ 2sin(\alpha)sin(\pi Jt)sin(2\beta)I_{1X}I_{2X}$
$- 2sin(\alpha)sin(\pi Jt)sin(2\beta)I_{1Z}I_{2Z}$
$- cos(\alpha)sin(\beta)cos(\pi Jt)I_{1X}$
$- 2cos(\alpha)sin(\beta)sin(\pi Jt)I_{1Y}I_{2Z}$
$- cos(\alpha)sin(\beta)cos(\pi Jt)I_{2X}$
$- 2cos(\alpha)sin(\beta)sin(\pi Jt)I_{1Z}I_{2Y}$
$- sin(\alpha)sin(2\pi Jt)(1 + cos(2\beta))I_{1X}I_{2Z}$
$- sin(\alpha)sin(2\pi Jt)(1 + cos(2\beta))I_{1Z}I_{2X}$
$+ sin(\alpha)cos^2(\pi Jt)I_{1Y}$
$+ sin(\alpha)cos^2(\pi Jt)I_{2Y}$
$- sin(\alpha)sin^2(\pi Jt)cos(2\beta)I_{1Y}$
$- sin(\alpha)sin^2(\pi Jt)cos(2\beta)I_{2Y}$

In σ_4 above, terms 1-4,6,8-10 are not observable. Therefore, the remaining key terms are:

$\sigma'_4 (y) =$
$- cos(\alpha)sin(\beta)cos(\pi Jt)I_{1X}$
$- cos(\alpha)sin(\beta)cos(\pi Jt)I_{2X}$
$+ sin(\alpha)cos^2(\pi Jt)I_{1Y}$
$+ sin(\alpha)cos^2(\pi Jt)I_{2Y}$
$- sin(\alpha)sin^2(\pi Jt)cos(2\beta)I_{1Y}$
$- sin(\alpha)sin^2(\pi Jt)cos(2\beta)I_{2Y}$

B) Different phase of the second pulse: α_x - t_{echo} - β_x - t_{echo} - acq

Steps 1 and 2 are the same as for β_y above.

3) Second pulse β_x

$I_Z \rightarrow cos(\beta)I_Z + sin(\beta)I_Y$
$I_X \rightarrow I_X$
$I_Y \rightarrow cos(\beta)I_Y - sin(\beta)I_Z$
$I_{1X}I_{2Z} \rightarrow I_{1X}(cos(\beta)I_{2Z} + sin(\beta)I_{2Y})$
$I_{1Z}I_{2X} \rightarrow I_{2X}(cos(\beta)I_{1Z} + sin(\beta)I_{1Y})$

$\sigma_3(x) = cos(\alpha)(cos(\beta)I_{1Z} + sin(\beta)I_{1Y})$
$+ cos(\alpha)(cos(\beta)I_{2Z} + sin(\beta)I_{2Y})$
$+ sin(\alpha)cos(\pi Jt)(cos(\beta)I_{1Y} - sin(\beta)I_{1Z})$
$+ sin(\alpha)cos(\pi Jt)(cos(\beta)I_{2Y} - sin(\beta)I_{2Z})$
$- 2sin(\alpha)sin(\pi Jt)I_{1X}(cos(\beta)I_{2Z} + sin(\beta)I_{2Y})$
$- 2sin(\alpha)sin(\pi Jt)(cos(\beta)I_{1Z} + sin(\beta)I_{1Y})I_{2X}$

4) Evolution under J-coupling

$I_Z \rightarrow I_Z$
$I_{1Y} \rightarrow cos(\pi Jt)I_{1Y} - sin(\pi Jt)2I_{1X}I_{2Z}$
$I_{2Y} \rightarrow cos(\pi Jt)I_{2Y} - sin(\pi Jt)2I_{1Z}I_{2X}$

$I_{1X} \rightarrow cos(\pi Jt)I_{1X} + sin(\pi Jt)2I_{1Y}I_{2Z}$
$I_{1X}I_{2Z} \rightarrow cos(\pi Jt)I_{1X}I_{2Z} + 0.5sin(\pi Jt)I_{1Y}$
$I_{1Z}I_{2X} \rightarrow cos(\pi Jt)I_{1Z}I_{2X} + 0.5sin(\pi Jt)I_{2Y}$

$\sigma_4(x) = (cos(\alpha)cos(\beta) - sin(\alpha)cos(\pi Jt)sin(\beta))I_{1Z}$
$+ (cos(\alpha)cos(\beta) - sin(\alpha)cos(\pi Jt)sin(\beta))I_{2Z}$
$+ cos(\alpha)sin(\beta)cos(\pi Jt)I_{1Y}$
$+ cos(\alpha)sin(\beta)cos(\pi Jt)I_{2Y}$
$- 2cos(\alpha)sin(\beta)sin(\pi Jt)I_{1X}I_{2Z}$
$- 2cos(\alpha)sin(\beta)sin(\pi Jt)I_{1Z}I_{2X}$
$- 2sin(\alpha)sin(\pi Jt)sin(\beta)I_{1X}I_{2Y}$
$- 2sin(\alpha)sin(\pi Jt)sin(\beta)I_{1Y}I_{2X}$
$+ sin(\alpha)cos(\beta)cos(2\pi Jt)I_{1Y}$
$+ sin(\alpha)cos(\beta)cos(2\pi Jt)I_{2Y}$
$- 2sin(\alpha)cos(\beta)sin(2\pi Jt)I_{1X}I_{2Z}$
$- 2sin(\alpha)cos(\beta)sin(2\pi Jt)I_{1Z}I_{2X}$

Terms 1,2,5-8,11,12 are not observable, which leaves:

$\sigma'_4(x) =$
$+ cos(\alpha)sin(\beta)cos(\pi Jt)I_{1Y}$
$+ cos(\alpha)sin(\beta)cos(\pi Jt)I_{2Y}$
$+ sin(\alpha)cos(\beta)cos(2\pi Jt)I_{1Y}$
$+ sin(\alpha)cos(\beta)cos(2\pi Jt)I_{2Y}$

C) Completing the phase cycle (EXORCYCLE)

(Note: phase cycling removes terms that are odd in β; also use: $1 - \cos(2\beta) = 2\sin^2(\beta)$):

$0.25(\sigma'_4(y) + \sigma'_4(-y) - \sigma_4'(x) - \sigma_4'(-x)) =$
$+ 0.5sin(\alpha)cos^2(\pi Jt)I_{1Y}$
$+ 0.5sin(\alpha)cos^2(\pi Jt)I_{2Y}$
$- 0.5sin(\alpha)sin^2(\pi Jt)cos(2\beta)I_{1Y}$
$- 0.5sin(\alpha)sin^2(\pi Jt)cos(2\beta)I_{2Y}$
$- 0.5sin(\alpha)cos(\beta)cos(2\pi Jt)I_{1Y}$
$- 0.5sin(\alpha)cos(\beta)cos(2\pi Jt)I_{2Y}$

$= 0.5sin(\alpha)[cos^2(\pi Jt) - sin^2(\pi Jt)cos(2\beta) - cos(2\pi Jt)cos(\beta)](I_{1Y} + I_{2Y})$
$= 0.5sin(\alpha)[cos(2\pi Jt)(1- cos(\beta)) + 2sin^2(\pi Jt)sin^2(\beta))](I_{1Y} + I_{2Y})$

The first term in the square brackets can be neglected because: (*i*) $\cos(\beta) \approx 1$ for small β; and (*ii*) averaging over the distribution of J values gives $\langle \cos(2\pi Jt) \rangle \approx 0$. Therefore:

$0.25(\sigma'_4(y) + \sigma'_4(-y) - \sigma_4'(x) - \sigma_4'(-x)) \approx sin(\alpha)sin^2(\pi Jt)sin^2(\beta))(I_{1Y} + I_{2Y})$

After averaging over J ($\langle \cos^2(\pi Jt) \rangle = 0.5$):

$0.25(\sigma'_4(y) + \sigma'_4(-y) - \sigma_4'(x) - \sigma_4'(-x)) \approx 0.5sin(\alpha)sin^2(\beta)(I_{1Y} + I_{2Y})$

The above equation can readily be generalized to the expression for the echo-detected signal intensity given in the main text.

3. *RF-Pulse Flip Angle Dependence*

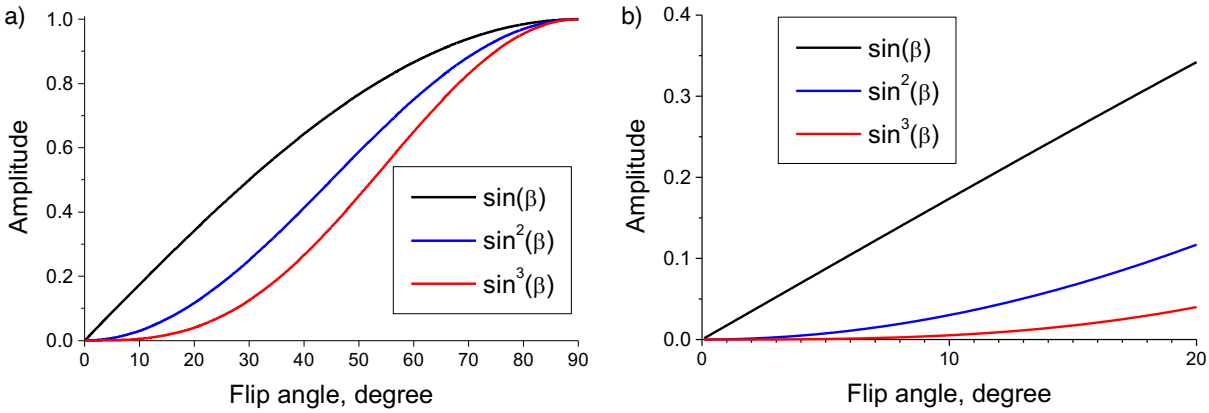

Figure S1: The expected dependence of NMR signal intensity as a function of the *rf*-pulse flip angle β for the pulse-acquire (black) and echo-detected (red) experiments. For the flip angle value used in the echo experiments ($\beta = 10°$), $\sin(\beta)/\sin^3(\beta) \approx 33$.

Figure S1a shows the expected dependence of the NMR signal intensity as a function of the *rf*-pulse flip angle β for the pulse-acquire and echo-detected experiments. Figure 1b shows this dependence in the small angle regime, *i.e.*, $\beta < 20°$. As can be clearly seen, a considerable amount (easily an order of magnitude) of NMR signal amplitude is lost for the case of small *rf*-pulse flip angles when using the echo-detected *rf*-pulse sequence.

4. ^{1}H DNP Build-Up

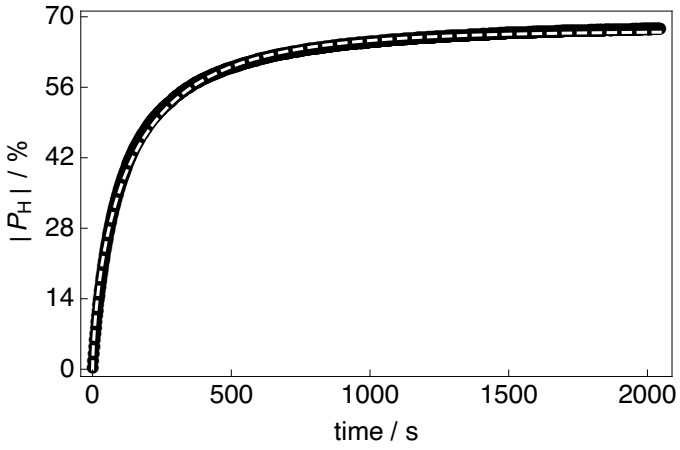

Figure S2: Experimental ^{1}H polarization $|P_H|$ build-up curve for sample **I** acquired at 7.05 T (^{1}H nuclear Larmor frequency = 300.13 MHz) and 1.2 K with a single transient (*rf*-pulse flip angle = 0.1°) as a function of the time $m \times t_{DNP}$ for the case of negative (emissive) DNP enhancement under microwave irradiation.

The experimental ^{1}H polarization $|P_H|$ build-up curve for sample **I** as a function of the microwave irradiation period $m \times t_{DNP}$ is shown in Figure S2. The ^{1}H polarization build-up curve was found to have a stretched exponential behaviour. The experimental data (black data points) are well fitted with a stretched exponential function (white dashed line) using a ^{1}H DNP build-up time constant denoted τ_{DNP}^{-}. Stretched exponential function: $A(1-\exp\{-(t/\tau_{DNP}^{-})^{\beta}\})$, where A is a fitting constant, τ_{DNP}^{-} is the ^{1}H DNP build-up time constant extracted from the above fitting procedure and β is the breadth of the distribution of ^{1}H DNP build-up time constants. The mean ^{1}H DNP build-up time constant $\langle\tau_{DNP}^{-}\rangle$ is calculated as follows: $\langle\tau_{DNP}^{-}\rangle = \tau_{DNP}^{-}\Gamma(1/\beta)/\beta$, where $\Gamma(1/\beta)$ is the gamma function. Sample **I** polarizes to $P_H \simeq$ -67.5% within ~34 min with a ^{1}H DNP build-up time constant of $\langle\tau_{DNP}^{-}\rangle$ = 196.7 ± 0.9 s and β = 0.67.

5. *Frequency Splitting ΔS vs. ^{1}H DNP Time*

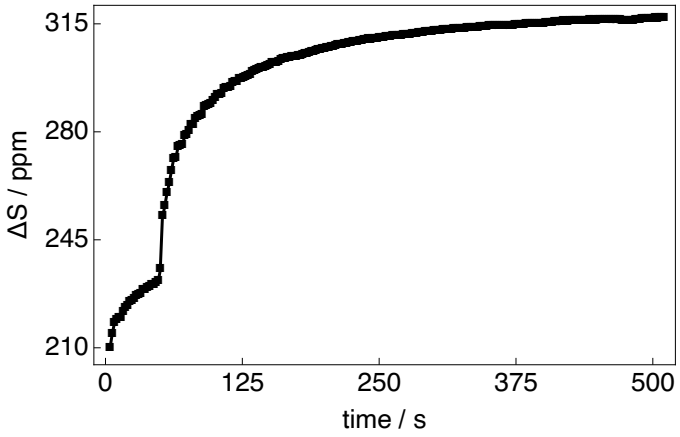

Figure S3: The observed separation of the peaks of the Pake doublet ΔS for sample **I** acquired at 7.05 T (^{1}H nuclear Larmor frequency = 300.13 MHz) and 1.2 K with a single transient per data point (α_{ϕ_1} = 0.1°; t_d = 5 μs) as a function of the time $m \times t_{DNP}$ for the case of microwave irradiation applied at the negative lobe of the DNP profile. Experimental data were obtained by implementing the *rf*-pulse sequence depicted in Figure 2a of the main text.

The trend of the observed splitting between the peaks of the Pake pattern ΔS increasing with increasing ^{1}H polarization is clearly shown as a function of the DNP build-up time in Figure S3. During the first ~46 s of the microwave irradiation period, *i.e.*, -21.3% < P_H < 0 %, the frequency splitting changes only slightly since the lineshape of the ^{1}H NMR spectrum is mostly controlled by the expected Pake pattern. After this point, there is a sharp jump in the value of ΔS as the false peak becomes more intense than the rightmost Pake horn (see Figure 3 of the main text). This is consequently associated with a substantial increase in the frequency splitting between the two main peaks of the ^{1}H NMR spectrum (by >85 ppm) before reaching an eventual plateau at longer microwave irradiation times (see Figure S3).

6. *Dead Time Induced Distortions*

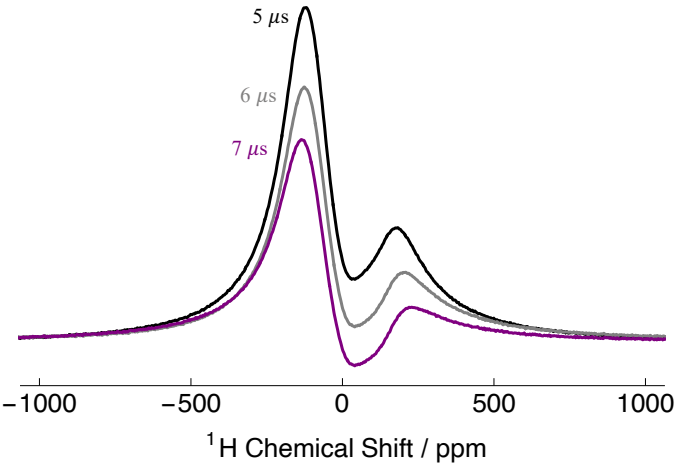

Figure S4: Experimental pulse-acquire ^{1}H NMR spectra for a sample of **I** acquired at 7.05 T (^{1}H nuclear Larmor frequency = 300.13 MHz) and 1.2 K with a single transient per data point (*rf*-pulse flip angle = 0.1°) as a function of the spectrometer dead time t_d for the case of P_H = -40.9%. Black: t_d = 5 μs; Grey: t_d = 6 μs; and Purple: t_d = 7 μs.

Figure S4 demonstrates the remarkable influence of the spectrometer dead time on the experimental ^{1}H NMR lineshape. There are two main effects: (*i*) increasing the dead time increases the difference in the relative ^{1}H NMR signal intensities for the two horns of the resolved Pake pattern; and (*ii*) the frequency separation between the horns of the Pake pattern increases with increasing dead time. It is also possible that the 5 μs spectrometer dead time used in the experiments (the shortest value allowed by the instrumentation) is a nominal value, while the actual value is in fact slightly larger.

7. *Pulse-Acquire Simulations*

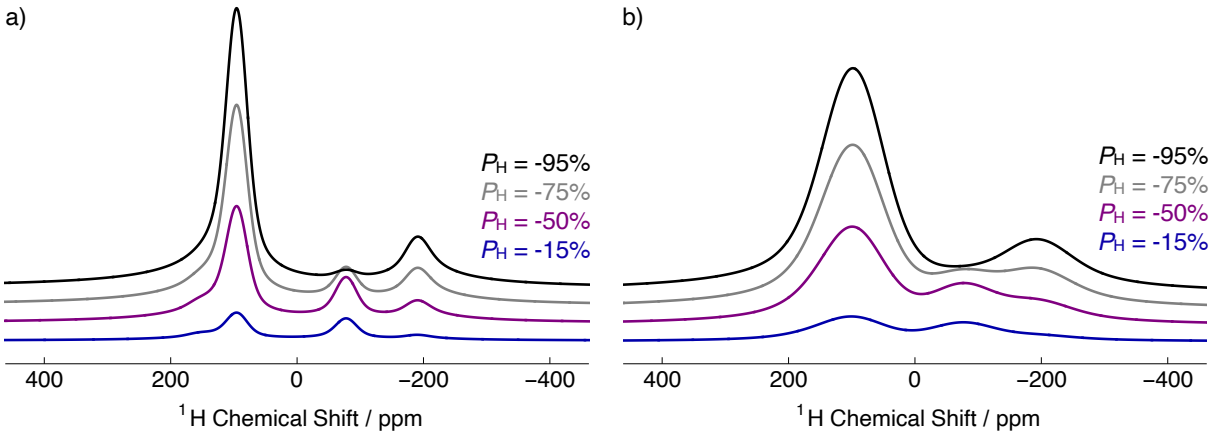

Figure S5: Simulated pulse-acquire ^{1}H NMR spectra (α_{ϕ_1} = 0.1°; t_d = 5 μs) as a function of the ^{1}H polarization level P_H. Black: P_H = -15%; Grey: P_H = -50%; Purple: P_H = -75%; and Blue: P_H = -95%. Spectrometer dead time: t_d = 5 μs. Gaussian line broadening with full-width at half-maximum height (FWHM) = a) 10 kHz and b) 30 kHz. The spin system parameters are those for an H_2O molecule and are the same as described in the main text.

Figure S5 shows simulated pulse-acquire ^{1}H NMR spectra as a function of the proton spin polarization level P_H. The intensity of these three peaks grows in a similar way to those of the experimental ^{1}H NMR spectra shown in Figure 3 of the main text, except that in the calculations of Figure S5a the linewidth was intentionally chosen to be relatively small to clearly reveal spectral transformations. Figure S5b shows the same ^{1}H NMR spectra simulated with more realistic linewidths. At lower levels of P_H, *i.e.*, -50% < P_H < -15%, the simulated spectrum resembles that of a traditional Pake doublet, although asymmetric due to the non-negligible ^{1}H spin polarization. At increased levels of the ^{1}H polarization, *i.e.*, -100% < P_H < -75%, the false peak governs the appearance of the spectrum.

From the simulated spectra shown in Figure S5a, it is evident that there are three major identifiable peaks. The leftmost peak corresponds to the leftmost horn of the Pake pattern. The smaller central peak corresponds to the rightmost horn of the Pake doublet. The rightmost peak is an artificial peak which arises when the ^{1}H polarization of the spin system becomes significant, whereby the inclusion of a dead time distorts the spectral lineshape. We note that this extra peak is not present when the FID detection dead time in simulations is set to zero, while the distortions become progressively more pronounced as both the artificial dead time and ^{1}H polarization are increased.

Although this overall trend is in agreement with the experimental data, the corresponding ^{1}H polarizations are not. For example, in the experimental data the intensity of the rightmost Pake horn and the false peak become equal at a ^{1}H polarization of ca. -21.3% (see Figure 3 of the main text). In the case of the simulated spectra, this observation does not occur until an approximate ^{1}H polarization of -75% (represented by the grey lineshape). At the corresponding level of ^{1}H polarization, the experimental data show a considerably greater lineshape distortion in the form of an exaggerated disparity in the relative peak intensities.

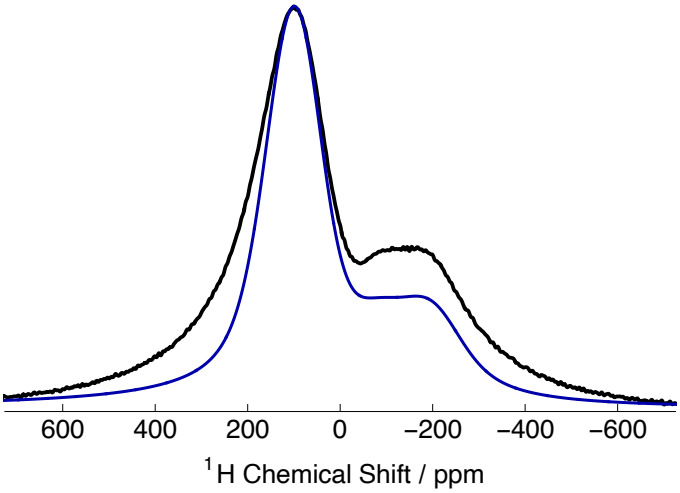

Figure S6: Experimental (black) and simulated (blue) ^{1}H NMR spectra (α_{ϕ_1} = 0.1°; t_d = 5 μs) at ^{1}H polarization levels of P_H = -21.3% and P_H = -75%, respectively. The experimental ^{1}H spin polarization P_H was measured by comparison with a thermal equilibrium ^{1}H NMR signal. Gaussian line broadening with full-width at half-maximum height (FWHM) = 37.5 kHz was used in the simulated spectrum.

Figure S6 shows a comparison between experimental (black) and simulated (blue) pulse-acquire ^{1}H NMR spectra at ^{1}H spin polarization levels of P_H = -21.3% and P_H = -75%, respectively. To emulate the detector dead time effects of the experimentally detected spectra, the initial portion of the calculated FID was eliminated before the Fourier transform. The simulated result is not a good match as compared with the experimental spectrum in terms of ^{1}H spin polarization P_H and lineshape: (*i*) A much higher ^{1}H spin polarization P_H is required in the simulated spectrum; and (*ii*) it is difficult to simulate the experimental ^{1}H NMR linewidth whilst preserving the notable features of the experimental NMR spectrum.

8. *Pulse-Acquire Spectra vs. Flip Angle*

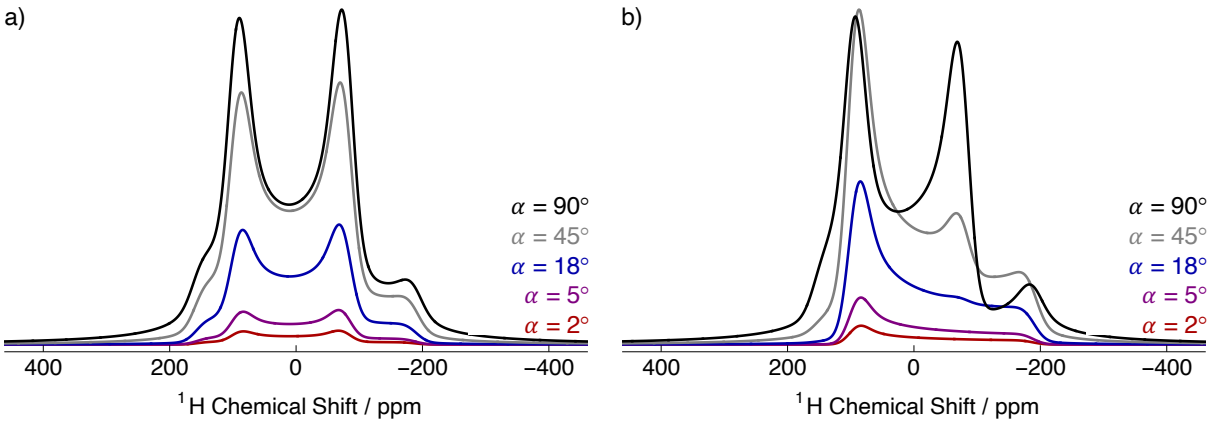

Figure S7: Simulated pulse-acquire ^{1}H NMR spectra at a) thermal equilibrium and b) P_H = -100% as a function of the *rf*-pulse flip angle α. Black: α = 90°; Grey: α = 45°; Purple: α = 18°; Blue: α = 5°; and Red: α = 2°.

Figure S7 shows simulated pulse-acquire ^{1}H NMR spectra at a) thermal equilibrium and b) P_H = -100% as a function of the *rf*-pulse flip angle α. At thermal equilibrium, the *rf*-pulse flip angle only influences the resulting ^{1}H NMR signal amplitude. However, at P_H = -100%, the *rf*-pulse flip angle has a remarkable influence on the lineshape of the resulting ^{1}H NMR spectrum. At low *rf*-pulse flip angles, *i.e.*, $\alpha \lesssim 18°$, the ^{1}H NMR lineshape resembles a pronounced Pake "horn" with a one-sided broad shoulder. However, as the *rf*-pulse flip angle is increased towards $\alpha = 90°$, the ^{1}H NMR spectrum begins to resemble the one acquired at thermal equilibrium.

9. Measurement of T_2

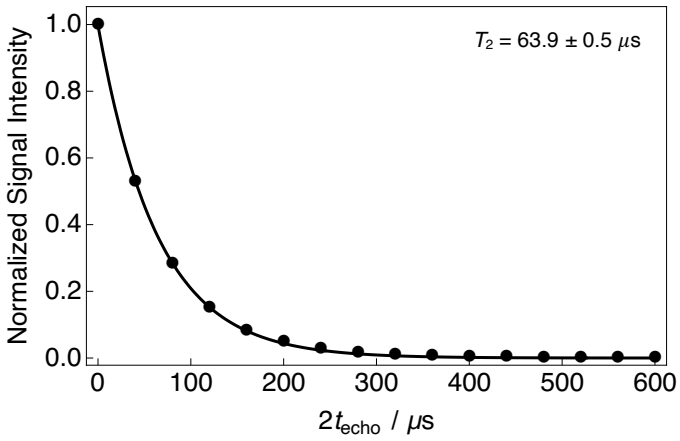

Figure S8: Experimental relaxation curve showing the decay of transverse magnetization for sample **I** acquired at 7.05 T (^{1}H nuclear Larmor frequency = 300.13 MHz) and 1.2 K with a single transient per data point. All signal amplitudes were normalized to the first data point. The fitted curve has a single exponential form.

The decay of transverse magnetization for sample **I** was measured by using a variant of the echo-based *rf*-pulse sequence depicted in Figure 2b of the main text, but with $\beta = 90°$. The echo-based *rf*-pulse sequence is repeated with incremented values of the delay time t_{echo} to monitor the relaxation of transverse magnetization. By fitting the integrated ^{1}H NMR signal decay as a function of the echo time $2t_{echo}$ the lifetime of transverse magnetization can be estimated.

The experimental decay curve showing the relaxation of transverse magnetization for sample **I** is presented in Figure S8. The decay of transverse magnetization was found to have a single-exponential behaviour. The experimental decay (black data points) is well fitted with a mono-exponential decay function (black solid line) using a sole relaxation time constant denoted T_2. Single mono-exponential decay function: $A\exp\{-t/T_2\}$, where A is a fitting constant and T_2 is the transverse magnetization relaxation time constant extracted from the above fitting procedure. The transverse magnetization relaxation time constant T_2 was measured to be: $T_2 = 63.9 \pm 0.5$ μs.